



Electrostatically Actuated X-Band Mesh Reflector with Bend-Formed Support Structure

John Z. Zhang,^{*} Harsh G. Bhundiya,[†] Kaleb D. Overby,[†] Fabien Royer,[‡]
Jeffrey H. Lang,[§] and Zachary C. Cordero[¶]

*Massachusetts Institute of Technology, Cambridge, Massachusetts 02139
and*

William F. Moulder,^{**} Sungeun K. Jeon,^{††} and Mark J. Silver^{‡‡}
MIT Lincoln Laboratory, Lexington, Massachusetts 02421

<https://doi.org/10.2514/1.A35914>

Increasing the size of radio frequency (RF) reflectors in space can enhance gain and spatial resolution in applications such as space-based communication and remote sensing. The size of current passive deployable reflectors is limited by a tradeoff between diameter and surface precision, which causes RF performance to degrade as size increases. A promising approach to overcome this tradeoff is to combine in-space manufacturing, which enables large structures, with distributed embedded actuation, which enables precise control over the reflector surface. Here we demonstrate a reflector antenna system that integrates these two technologies, using a candidate in-space manufacturing process, termed “Bend-Forming,” with embedded electrostatic actuators. We design and fabricate a 1-m-diam prototype of an electrostatically actuated X-band reflector with a knitted gold-molybdenum mesh as the reflector surface, carbon-fiber-reinforced plastic booms as electrodes, and a truss support structure fabricated with Bend-Forming. We characterize the RF performance of this reflector, successfully demonstrating i) control over a wide range of focal lengths by suppressing a pull-in instability and ii) beam steering over an angular range of 4.2° via asymmetric electrostatic actuation. This work lays the foundation for future space communication and remote sensing technologies, offering a scalable solution to enhance RF performance through in-space manufacturing and precision control.

Nomenclature

A	= area, m ²	k	= spring constant, N/m
b	= damping coefficient, N·s/m	L_b	= bay sidelength, m
C_0	= capacitance, F	L_t	= triangle sidelength, m
D	= reflector diameter, m	m	= mass, kg
d	= gap distance, m	N_{attach}	= mesh attachment points
E	= electric field, V/m	P	= pressure, Pa
E_Y	= Young's modulus, GPa	Q	= charge, C
F_R	= radial reaction force, N	R	= resistance, Ω
F_V	= vertical reaction force, N	T	= mesh tension, N/m
f	= focal length, m	V	= electric potential, V
f/D	= ratio of focal length to diameter	V_b	= bias voltage, V
G	= gain, dBi	ν	= Poisson's ratio
HPBW	= half-power (3-dB) beamwidth, °	v_c	= control voltage, V
		w	= membrane displacement, m
		x	= displacement, m
		δ	= mesh displacement (near center), m
		ζ	= damping ratio
		η	= efficiency
		τ	= electromechanical bandwidth ratio
		ϕ	= electric potential, V
		φ	= azimuth angle, °
		ϵ_0	= vacuum permittivity, F/m
		ω_0	= natural frequency, rad/s

Received 29 October 2023; revision received 5 March 2024; accepted for publication 18 March 2024; published online Open Access 29 April 2024. Copyright © 2024 by the American Institute of Aeronautics and Astronautics, Inc. All rights reserved. All requests for copying and permission to reprint should be submitted to CCC at www.copyright.com; employ the eISSN 1533-6794 to initiate your request. See also AIAA Rights and Permissions www.aiaa.org/randp.

*Graduate Student, Department of Mechanical Engineering, 77 Massachusetts Avenue, Student Member AIAA.

†Graduate Student, Department of Aeronautics and Astronautics, 77 Massachusetts Avenue, Student Member AIAA.

‡Postdoctoral Researcher, Department of Aeronautics and Astronautics, 77 Massachusetts Avenue; currently Assistant Professor, Cornell University Sibley School of Mechanical and Aerospace Engineering, 616 Thurston Avenue, Ithaca, NY. Member AIAA.

§Vitesse Professor, Department of Electrical Engineering and Computer Science, 77 Massachusetts Avenue.

¶Edgerton Career Development Assistant Professor, Department of Aeronautics and Astronautics, 77 Massachusetts Avenue; zcordero@mit.edu. Member AIAA (Corresponding Author).

**Technical Staff, RF Technology, 244 Wood Street.

††Technical Staff, Structural and Thermal Engineering, 244 Wood Street. Senior Member AIAA.

‡‡Assistant Group Leader, Mechanical Engineering, 244 Wood Street. Associate Fellow AIAA.

I. Introduction

INCREASING the size of radio frequency (RF) reflectors used in space-based communication and sensing applications can improve key performance metrics such as gain and spatial resolution. Current state-of-the-art reflectors, such as the Northrop Grumman Astromesh, are passive deployable devices that are packaged into a small form-factor for launch and then deployed into a larger configuration on orbit. The size of such reflectors is limited by packaging constraints [1,2] and by a tradeoff between size and surface precision. This tradeoff is highlighted in Fig. 1 and arises from fabrication errors [3] and various effects encountered on orbit (disturbance loads, thermal distortion [4]). These considerations have limited the practical size of modern deployable RF reflectors to several tens of meters, with a maximum diameter of order 20 m currently deployed

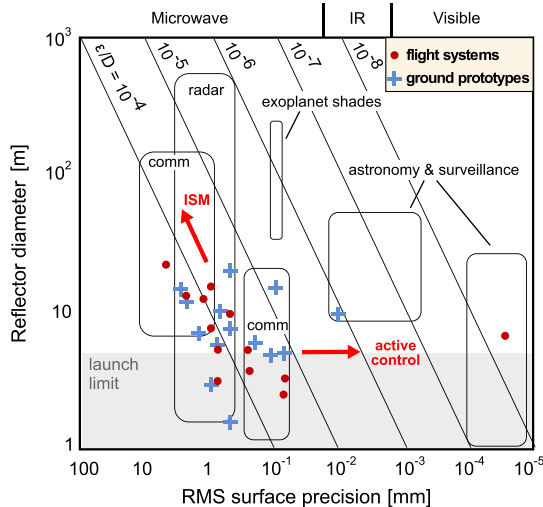


Fig. 1 Diameter and root-mean-square (RMS) surface precision of modern deployable space reflectors compared against requirements for specific applications (adapted from [1]). In-space manufacturing (ISM) and active control via electrostatic actuation may enable larger reflectors with improved precision.

in geosynchronous orbit [5]. Other limitations of current passive deployable reflectors include a fixed reflector pattern, slow slew rates due to the large inertia of the supporting structure [6], and cross-polarization interference from the faceted reflector surface [7].

A candidate approach to circumvent packaging constraints on reflector size is to robotically fabricate structures on orbit from raw feedstock via in-space manufacturing (ISM). This approach can be used to fabricate structures optimized for the space environment with dimensions larger than current deployable systems. A wide range of feedstock materials and processing methods have been proposed for ISM, including melt-based additive manufacturing of metallic and fiber-reinforced composite feedstocks [8,9]; extrusion of fiber-reinforced plastics [10]; and deformation processing of metals [11,12]. A recent comparison of these processes [13] showed that deformation processing is an especially promising ISM method for fabricating large structures due to its low specific energy consumption. However, a challenge with ISM processes (including deformation processes) is that the error stack-up of individual fabrication steps degrades the accuracy of the final structure [12]. Thus, while ISM can make extremely large reflectors (cf. Fig. 1), the surface precision of ISM reflectors will still be limited by the same underlying physics as conventional passive deployables, with a tradeoff between size and surface precision.

Breaking this tradeoff to achieve large, *precise* reflectors requires combining ISM with actuators, which can adjust the reflector surface to correct errors. A promising actuation modality for this purpose is electrostatic actuation. This method entails placing an electrode array (command surface) at a predetermined distance from the conductive reflector surface. By applying a bias voltage across these surfaces, the reflector can be drawn into a desired shape. Electrostatic actuation is low power and low mass, and it can precisely contour the reflector shape by adjusting the individual control voltages of the electrode array [14]. There have been several ground demonstrations of electrostatically actuated reflectors, including closed-loop stabilization of higher-order modes on a subscale 1.2-m-diam reflector [15,16], open-loop control on a larger system (4.88-m-diam) with different command surface electrode configurations [17], and electrostatic actuation of a retrofitted Astromesh reflector [18]. These studies collectively demonstrate *in situ* correction of surface errors and also suggest new capabilities such as beam shaping and beam steering.

Comparing electrostatic actuation with other proposed methods for active deformable RF/optical apertures, such as cable shape-control [19], piezoelectric actuation [20], among others [21,22], highlights several performance advantages of electrostatic actuation and its ease of implementation with ISM structures. Clarricoat and

Zhou demonstrated cable shape-control of a 0.85-m-diam mesh reflector using 78 control points tensioned through cords attached to motorized actuators [19]. A major challenge of this cable shape-control method is pillowowing of the mesh, which leads to loss in gain and additional side lobes. In comparison, electrostatic actuation is a distributed method that avoids the pillowowing effect through the spatial filtering of Laplace's equation for electrostatics and the low-pass mechanical filtering nature of the membrane. Other techniques, like piezoelectric actuation using a piezofilm bimorph to alter the shape of a cylindrical reflector, as reported by Washington [20], are limited in deflection, thus reducing the range of achievable antenna patterns. There are further methodologies for surface control methods such as magnetostrictive actuation [23], actuation using shape memory alloys [24] or pressurized membranes [25], and thermoyield actuation [26], but these are not always candidates considered for flight systems, and some can be classified as shape correction schemes rather than shape control, meaning large excursions to other possible shapes. Finally, electrostatic actuation should be relatively straightforward to implement with ISM processes since it does not require mechanical attachments to the compliant, difficult-to-handle mesh reflector surface and since the command surface electrodes can be applied to the rigid support structure during fabrication.

In this paper, we report a ground demonstration of an electrostatically actuated mesh reflector, which combines the unique capabilities of a candidate ISM process, Bend-Forming [12], and electrostatic actuation with closed-loop control. The 1-m-diam prototype reflector presented here comprises a knitted mesh reflector surface, carbon-fiber-reinforced plastic (CFRP) booms as electrodes, and a Bend-Formed support structure. RF measurements of this prototype reflector demonstrate i) control over a wide range of focal lengths by suppressing a pull-in instability and ii) beam steering over an angular range of 4.2° via asymmetric electrostatic actuation. This work demonstrates the critical function of an electrostatically actuated mesh reflector and highlights new capabilities enabled through electrostatic actuation—selective focusing and beam steering—which can be combined with ISM to enable a new class of ultralarge mesh reflectors for space-based sensing and communication.

II. Methods

Figure 2 shows the electrostatically actuated reflector prototype and its three main components: a 1-m-diam knitted gold-molybdenum mesh with 40 openings per inch (OPI); a Bend-Formed support structure fabricated from 1 mm steel wire; and a command surface of CFRP electrodes. To contour the mesh reflector, we apply a bias voltage between the mesh and the command surface using a high-voltage (HV) power supply. The resulting electrostatic force between the mesh and the command surface pulls the mesh toward the electrodes. There is a pull-in instability at a critical bias voltage, above which the attractive electrostatic force between the mesh and command surface overcomes the restoring membrane tension in the mesh. To stabilize this instability at large mesh displacements, we dynamically adjusted the control voltage using closed-loop control with feedback from a laser displacement sensor focused on the center of the reflector. High-bandwidth modulation of the control voltage is accomplished using a ±5 kV amplifier driven by a proportional-integral controller.

Asymmetric deformation of the reflector surface (i.e., beam steering) is accomplished by using the amplifier to adjust voltage on half of the command surface while the other half is grounded. Sections II.A and II.B further describe the design and fabrication of the truss support structure and CFRP electrodes. More details on the electrostatic actuation and control schemes are provided in Sec. II.C.

A. Bend-Formed Support Structure

Here we describe the design and fabrication of the Bend-Formed support structure for the prototype shown in Fig. 2. The key design requirement for the support structure is to provide radial and vertical reaction forces at the mesh attachment points as the mesh deflects toward the electrodes in response to the applied bias voltage.

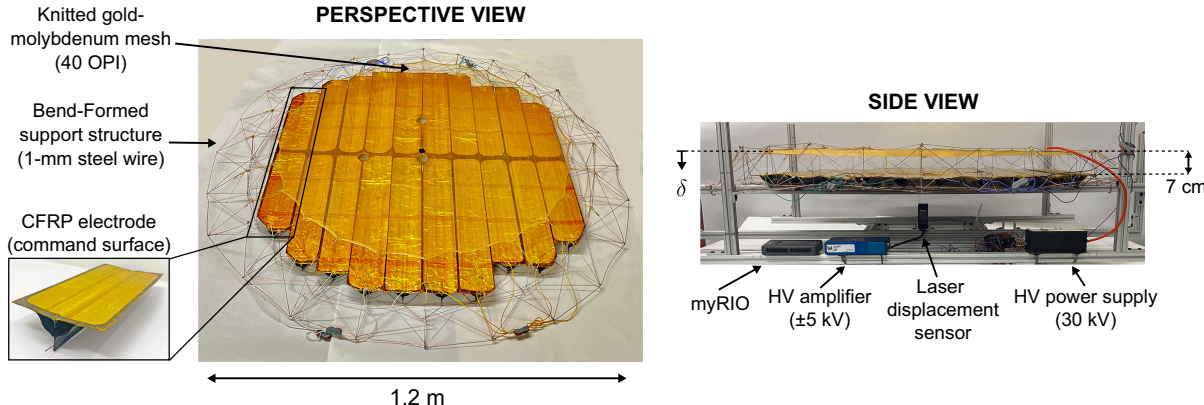


Fig. 2 Electrostatically actuated mesh reflector. A bias voltage applied between the mesh and command surfaces deforms the mesh into a curved surface. A laser displacement sensor measures mesh deflection (δ) near the center, and a high-bandwidth amplifier enables closed-loop actuation.

Modeling the mesh as a thin circular membrane with diameter D and uniform tension T (N/m), the radial reaction force (F_R) at each attachment point is

$$F_R = \frac{\pi D T}{N_{\text{attach}}} \quad (1)$$

where N_{attach} is the number of attachment points around the mesh circumference. Additionally, modeling the mesh and command surfaces as flat parallel plates separated by a gap distance d (further described in Sec. II.C), the vertical reaction force F_V on the support structure balances the electrostatic force on the mesh, expressed as

$$F_V = \frac{1}{2} \epsilon_0 \left(\frac{V}{d} \right)^2 \frac{A}{N_{\text{attach}}} \quad (2)$$

where ϵ_0 is the vacuum permittivity, V is the voltage applied between the mesh and command surface, A is the electrode area, and d is the gap distance. For a given maximum mesh tension T_{\max} and a maximum bias voltage V_{\max} , the support structure must be designed to not buckle under the maximum radial and vertical forces given by Eqs. (1) and (2). The support structure must also be designed to provide a sufficient gap distance between the mesh and command surfaces so that the desired reflector shape can be achieved without collision and dielectric breakdown between the two surfaces.

Considering these design requirements, we pursue a structural concept consisting of a ring truss that attaches to the mesh around its circumference and an inner triangular grid that supports the electrodes of the command surface. The ring truss consists of bays with an isosceles right triangle cross section and alternating diagonals, as depicted in Fig. 3. For our prototype, we chose $N_{\text{attach}} = 24$ mesh attachment points, a bay side length of $L_b = 0.16$ mm, a triangle cross section of $L_t = 0.1$ m, and a gap distance of $d = 0.1$ m. These dimensions were chosen to support a mesh surface

with diameter $D = 1$ m, a maximum voltage of $V_{\max} = 30$ kV, and a representative maximum mesh tension. To verify that the radial and vertical buckling loads of the support structure were greater than the corresponding forces given by Eqs. (1) and (2), a finite element analysis was conducted in Abaqus (2021, Dassault Systemes), using beam elements (B31) and a buckling eigenvalue analysis step. Modeling the structure with 1-mm steel wire ($E_Y = 200$ GPa, $\nu = 0.29$) and assuming rigid joints at the nodes, radial and vertical loads were applied to the mesh attachment points with pinned boundary conditions at the bottom nodes of the ring. This analysis resulted in the critical radial and vertical buckling loads $F_R^* = 1.69$ N and $F_V^* = 15.0$ N, which were deemed sufficient to support the radial and vertical forces with a safety factor of 1.5.

The structural concept of Fig. 3 was fabricated using the deformation process of Bend-Forming, which combines computer numerical control (CNC) wire bending with mechanical joints to construct reticulated structures from wire feedstock [12]. A bend path was found that continuously traverses all edges of the geometry and was converted to fabrication instructions for a CNC wire bender. For the prototype shown in Fig. 2, separate bend paths were computed for the ring truss and inner triangular grid and combined to form a single bend path for the full structure. The corresponding fabrication instructions were implemented on the DI Wire Pro, a desktop CNC wire bender [27], with 1-mm-diam steel wire as the feedstock. Finally, solder joints were added to the nodes, resulting in the support structure shown in Fig. 2. Due to fabrication defects of the Bend-Forming process (e.g., feed length error, angular error, and nonzero strut curvature), the final geometry of the truss support structure contained defects such as buckled struts and nonplanar mesh attachment points. The mesh was attached to the top nodes of the ring truss via cables, and the electrodes of the command surfaces were attached to the inner triangular grid via wire slots (further described in Sec. II.B). The attachment of the CFRP electrodes resulted in a final gap distance between the mesh and command surfaces of $d \approx 7$ cm (see Fig. 2) before actuation. Additionally, a small hole was cut in an electrode near the center of the prototype to allow measurement of the mesh displacement with a laser displacement sensor.

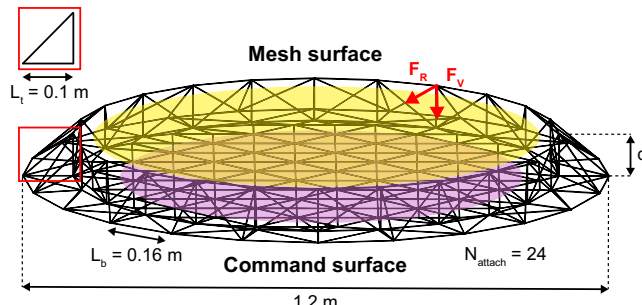


Fig. 3 Truss support structure for an electrostatically actuated mesh reflector. A ring truss supports the mesh (gold) around its circumference, and a triangular grid supports electrodes on the command surface (purple).

B. Command Surface

The command surface sits opposite the mesh such that when an electric potential is applied between the two surfaces, the electrostatic force deforms the mesh into a curved shape. A nominally flat command surface was adopted for simplicity in these initial experiments. The Bend-Formed support structure alone does not provide a suitable command surface since 1) the porosity of a wire frame command surface has limited actuation force due to its low capacitance; 2) it has low out-of-plane stiffness and thus easily deflects in the direction of the electric field; 3) it does not readily permit individually addressable electrodes necessary for asymmetric actuation; and 4) the wire backbone creates an electric field concentration that promotes dielectric breakdown [28]. Thus, we instead implemented a command surface made from CFRP booms, as shown in Fig. 4. These booms increase the

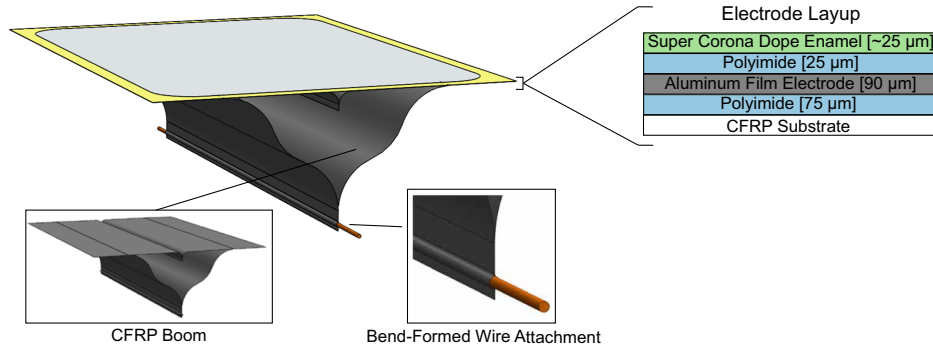


Fig. 4 Command surface electrode consisting of a CFRP boom with an aluminum film electrode and dielectric layup.

global stiffness of the structure and act as individually addressable planar electrodes. The boom cross sections were designed to have a large planar area while being flattenable and easily attached to the wireframe structure, thus making them compatible with Bend-Forming. To maintain consistent, predictable electrostatic pressure, the booms were optimized to minimize out-of-plane deflection. Finite element simulations with Abaqus predicted a worst-case maximum deflection of 1.6 m at the midspan of a boom under an electrostatic pressure of 100 Pa, corresponding to the maximum bias voltage of 30 kV. The booms were fabricated using a silicone molding, out-of-autoclave manufacturing method [29,30].

We applied a layup of various conducting and nonconducting materials to the CFRP booms to enable their use as individually addressable electrodes. The layup and individual layer thicknesses are given in Fig. 4. This layup insulated the electrode from the CFRP and provided sufficient dielectric strength to prevent breakdown over the desired range of voltages. Table 1 compares the electric field between the mesh and command surfaces with the dielectric strengths of the various materials within the gap distance, ignoring fringing effects at the edges of the electrode and modeling the two surfaces as parallel plates. Breakdown in air was predicted at a gap distance of approximately 1 cm, when the field strength exceeds 30 kV/cm (the dielectric strength of air at 0°C and 760 Torr) [31]. Experimentally, breakdown occurred at gap distances of 1.5 cm between 24 and 27 kV. This discrepancy was likely due to field concentration effects at the edges of the command surface electrodes. We found that polyimide and dielectric enamel suppressed breakdown at the electrode edges, where electrical discharge was visibly identified to occur.

The electrode pattern formed by parallel booms had two drawbacks. First, the electrode pattern permitted the command surface potential to vary over 10 segments in one direction and only two segments in the other. Second, the parallel organization of CFRP booms created an orthotropic structure where the bending stiffness along the axis of the booms was much greater than in the transverse direction. Instead of the parallel electrode pattern, a pattern with concentric rings of rectangular electrodes may improve upon both of these drawbacks, permitting equivalent degrees of freedom in the two primary axes and creating a structure with quasi-isotropic stiffness.

C. Electrostatic Actuation

In equilibrium, the electric field between the mesh and the command surface is governed by Laplace's equation for electrostatics, while the displacement field is governed by a force balance between electrostatic attraction and the restoring mesh tension. We approximate the key behaviors of this system using a single-degree-of-freedom (sdof) model illustrated in Fig. 5.

Table 1 Electrode layup electric field and dielectric strength

Medium	Electric field, kV/cm	Dielectric strength, kV/cm
Polyimide	9	1600
Corona Dope Enamel	8	1500–3000
Air Gap	30	30

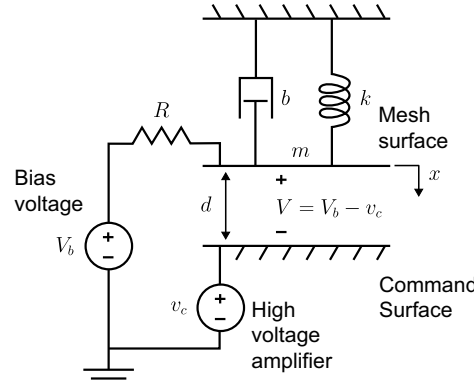


Fig. 5 Single-degree-of-freedom electrostatic actuator.

The dynamics of this sdof system are governed by

$$\underbrace{m\ddot{x} + b\dot{x} + kx}_{\text{mechanical}} = \frac{Q^2}{2\epsilon_0 A} \quad \text{and} \quad \underbrace{\dot{Q}}_{\text{electrical}} = \frac{1}{R} \left(V - \frac{Q(d-x)}{\epsilon_0 A} \right) \quad (3)$$

where m is the mass, b is the damping coefficient, k is the spring constant, Q is the charge on the mesh, A is the electrode area, R is resistance, d is the initial gap, and $V = V_b - v_c$ is the voltage difference across the mesh and the command surface. The parameters m , b , and k in the sdof model are effective properties, distinct from the areal mass, damping, and stiffness of the physical reflector system. These expressions can be nondimensionalized using the gap distance (d), natural frequency of the spring (ω_0), and the charge and voltage at pull-in (q^* , v^*):

$$\hat{x} = \frac{x}{d}, \quad \hat{t} = \omega_0 t, \quad \hat{q} = \frac{Q}{q^*}, \quad \hat{v} = \frac{V}{v^*} \quad (4)$$

Here $\omega_0 = \sqrt{(k/m)}$, $q^* = (3/2)C_0v^*$, and $v^* = \sqrt{(8kd^2/27C_0)}$, where $C_0 = (\epsilon_0 A/d)$ is the initial capacitance of the parallel plate capacitor. The voltage v^* is the classic pull-in voltage of the sdof system [32], corresponding to the voltage above which the effective spring constant of the system becomes negative. For simplicity in what follows, we drop the hats for the nondimensional variables. The resulting nondimensionalized coupled differential equations that govern the deformation and charging of the mesh surface with time are

$$\ddot{x} + 2\zeta\dot{x} + x = \frac{1}{3}q^2 \quad \text{and} \quad \tau\dot{q} + (1-x)q = \frac{2}{3}v \quad (5)$$

where $\zeta = (b/2m\omega_0)$ is the damping ratio and $\tau = \omega_0 RC_0$ is the ratio of bandwidths for the mechanical and electrical dynamics. If the resistance vanishes or the capacitance is small, then the charge dynamics disappear ($\tau = 0$) and we recover the equation

$$m\ddot{x} + b\dot{x} + kx = \frac{1}{2}\epsilon_0 A \frac{1}{(d-x)^2} V^2 \quad (6)$$

which considers only dynamics of the mechanical system with a nonlinear voltage-controlled force. Including charge as an additional state variable is useful for analyzing disturbances due to interactions with the space environment and current limits of the amplifier.

Using the following choices of states, $x_1(t) = x(t)$, $x_2(t) = \dot{x}(t)$, and $x_3(t) = q(t)$, the final nondimensional state space equations are then

$$\dot{\mathbf{x}}(t) = \begin{pmatrix} \dot{x}_1(t) \\ \dot{x}_2(t) \\ \dot{x}_3(t) \end{pmatrix} = \begin{pmatrix} x_2 \\ -2\zeta x_2 - x_1 + \frac{1}{3}x_3^2 \\ -\frac{1}{\tau}(1-x_1)x_3 + \frac{2}{3\tau}v \end{pmatrix} \quad (7)$$

The stationary points X_i relating charge to displacement are satisfied by $X_1 = (1/3)X_3^2$ and $X_2 = 0$, which can be re-expressed in terms of voltage as

$$v = \sqrt{\frac{27}{4}}\sqrt{x}(1-x) \quad (8)$$

We use uppercase X_i here to denote the equilibria distinguishing them from the state variables x_i . The stability of the system can be assessed by linearizing Eq. (7) about each operating point and determining the sign of the eigenvalues from the linearized state matrix. The set of equilibria described by Eq. (8) is stable below $x < 1/3$ and unstable for larger displacements (see black line in Fig. 6). For the sdof model, the critical pull-in displacement is always 1/3 of the gap distance.

In continuum systems, such as the electrostatically actuated membranes of present interest, the pull-in displacement is larger than that of the sdof model, and the shape of the pull-in curve differs as well [32]. For the membrane, the critical pull-in displacement is around 1/2 of the gap distance, and the final normalized voltage at touchdown is 4/9 [33,34]. The differences between the sdof and membrane pull-in behaviors are highlighted in Fig. 6, which shows the normalized displacement of the sdof model as a function of applied voltage, calculated using Eq. (8), as well as an electromechanically coupled finite element simulation in COMSOL Multiphysics of an electrostatically actuated membrane, similar to our experimental prototype. After pull-in, displacement increases with a decreasing voltage difference between the mesh and command surface. In practice, the operating limits of the 1 m prototype in the unstable region are

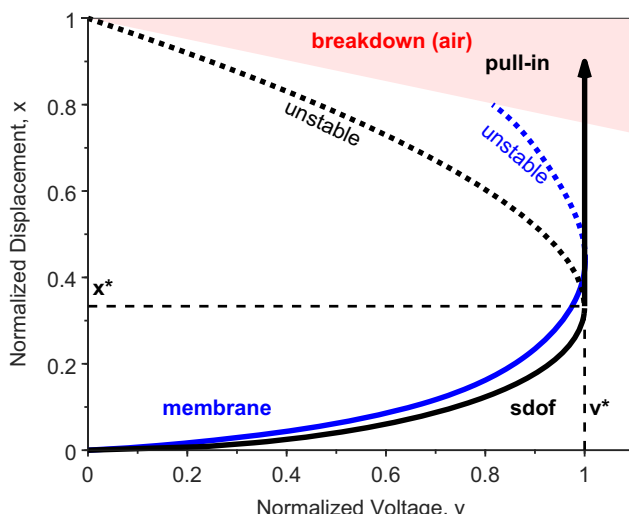


Fig. 6 Normalized pull-in curves for a single-degree-of-freedom (black) and membrane (blue) electrostatic actuator. The pull-in point is indicated as (v^*, x^*) and occurs at a deeper depth for the membrane. The red region indicates where electrical breakdown occurs in air (30 kV/cm).

ultimately limited by electrical breakdown. The red region indicates the high likelihood of electrical discharge in air defined using 30 kV/cm as the slope.

An important design consideration is how the voltage required to deflect the mesh varies with the reflector size. We develop a scaling relation for the voltage requirements by considering the pull-in behavior in the sdof model. From Eq. (4), the pull-in voltage for the sdof electrostatic actuator scales as

$$v^* \propto \sqrt{\frac{kd^2}{C_0}} \quad (9)$$

The capacitance between the electrodes, $C_0 = \epsilon_0(A/d)$, is directly proportional to diameter D because the initial gap distance d must grow linearly with diameter to achieve the same f/D . The effective spring constant of the mesh k can be estimated from the pressure applied over an area A and the center displacement $\delta = w(r=0)$, as

$$k \equiv \frac{PA}{\delta} = \frac{16TA}{D^2} \quad (10)$$

which shows that k scales linearly with tension. Substituting into Eq. (9), assuming a constant membrane tension T , we find

$$v^* \propto \sqrt{D} \quad (11)$$

Hence the pull-in voltage, which represents the maximum voltage needed to actuate the membrane to the same parabolic shape, scales with the square root of the membrane diameter.

A final point of discussion is that using electrostatic actuation to form the reflector into an ideal paraboloid requires a nonuniform bias voltage on the command surface. The vertical displacement w of a membrane with uniform tension T under a pressure load p is described by

$$\nabla^2 w = \frac{p}{T} \quad (12)$$

The solution to Eq. (12) for a circular membrane with radius R , a pinned boundary condition, and a uniform pressure P is a paraboloid, i.e.,

$$w = \frac{PR^2}{16T} \left[1 - \left(\frac{r}{R} \right)^2 \right] \quad (13)$$

However, in our experiments, we control voltage, not electric field. Thus, when a uniform bias voltage is applied to deflect the mesh, the electric field varies with radius and is highest at the mesh nadir, where the mesh is closest to the electrode. Under voltage control, when the air gap is small compared to the diameter [35], the resulting electrostatic pressure can be approximated as

$$p = \frac{1}{2}\epsilon_0 \frac{v^2}{(d-w)^2} \quad (14)$$

where v is an applied voltage that can vary with location on the membrane. Combining Eqs. (12) and (14) yields a nonlinear expression whose solution for spatially uniform v and small displacements is nearly parabolic. Deviation from a paraboloid grows as the voltage increases and the mesh deflects into a deeper configuration.

D. Controller Implementation

Figure 7 shows the digital control scheme used for our prototype. The mesh was stabilized using a proportional-integral controller implemented on a field programmable gate array (FPGA; myRIO-1900, National Instruments). While our experiments used a controller loop rate of 100 kHz, we expect a loop rate of 1 kHz is sufficient to stabilize the first mode instability, given that the fundamental frequency of the mesh was around 100 Hz. This slower loop rate is in line with flight-qualified computing capabilities and the sampling rate of noncontact metrology techniques. For the closed-loop reference,

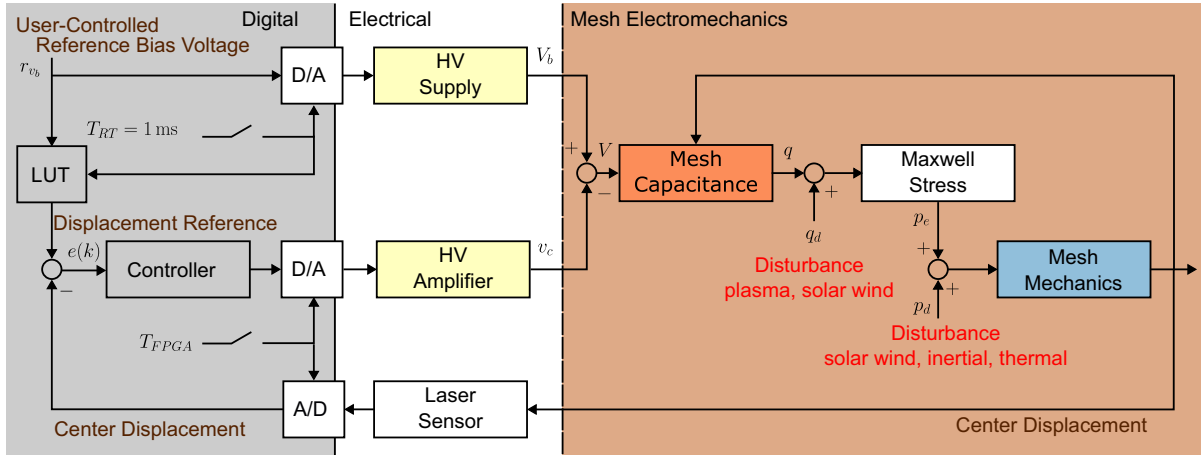


Fig. 7 Block diagram of the control scheme for closed-loop electrostatic actuation.

a look-up table (LUT) was used to interpolate the pull-in curve to decide the proper displacement given an input bias voltage. The HV electronics included a HV power supply (AHV24V30KVR5MAW, Analog Technologies) capable of 30 kV output with a slow slew rate and a fast HV amplifier (5HVA24-BP1, UltraVolt Advanced Energy) capable of ± 5 kV with a bandwidth greater than 1 kHz. A Keyence laser displacement sensor (LK-G3001 and LK-G152, Keyence) with a sampling rate of 1 kHz was used to measure the mesh displacement for feedback control. The gains were chosen based on the sdof model and tuned on the real 1 m prototype. The maximum center deflection was limited by electrical breakdown of air.

The block diagram in Fig. 7 illustrates how the voltages sum across the mesh and command surface and how the generalized mesh capacitance $Q = \tilde{Q}(V, x)$ gives rise to a charge. This charge is then converted to a force or moment via the Maxwell stress tensor that acts on the mesh, resulting in a displacement. In this diagram, nonlinearity arises in the Maxwell stress and electromechanical coupling. It is also possible to include disturbances from sources such as plasma, thermal loads, and solar wind, which will affect stability, noise (i.e., surface precision), and power draw.

III. Results and Discussion

We assessed the performance of our reflector prototype through RF measurements at the Compact Range Facility of MIT Lincoln Laboratory. The testing setup in Fig. 8 shows the reflector prototype attached to a rotator assembly. Plane radiation patterns were collected by rotating the reflector in the azimuth direction (ϕ) and measuring the reflected amplitude and phase of the signal. All radiation patterns were measured at 10 GHz (X-band), with a standard 8.2–12.4 GHz

feed horn and an angular resolution of 0.5° for focusing experiments and 1° for beam steering experiments. During each measurement, the mesh surface was deformed into a curved shape using electrostatic actuation, via the actuation and control schemes presented in Secs. II.C and II.D. The laser displacement sensor and HV power electronics were placed behind the reflector prototype (see Fig. 2) and attached to the support structure. Below, we present the results obtained with open- and closed-loop electrostatic actuation as well as beam steering.

A. Open- and Closed-Loop Electrostatic Actuation

The mesh surface was electrostatically actuated into a curved shape by applying a potential difference across the mesh and command surface with both open-loop and closed-loop controllers. Figure 9 shows the mesh displacement δ measured using the laser displacement sensor versus the applied voltage. There is a nonlinear increase in displacement with voltage as the mesh approaches the pull-in instability ($V^* \approx 26.2$ kV, $\delta^* \approx 38$ mm). The controller is activated when the displacement crosses the threshold displacement δ^* . Beyond this displacement, the HV amplifier adjusts the command surface voltage to stabilize the system at a given reference value. The reference displacement past pull-in is computed using an interpolated LUT (see Sec. II.C). On this stabilized path, the displacement continues to increase with a decreasing voltage difference. This behavior is demonstrated in the experimental measurements of mesh displacement for different voltages summarized in Fig. 9, which show that the

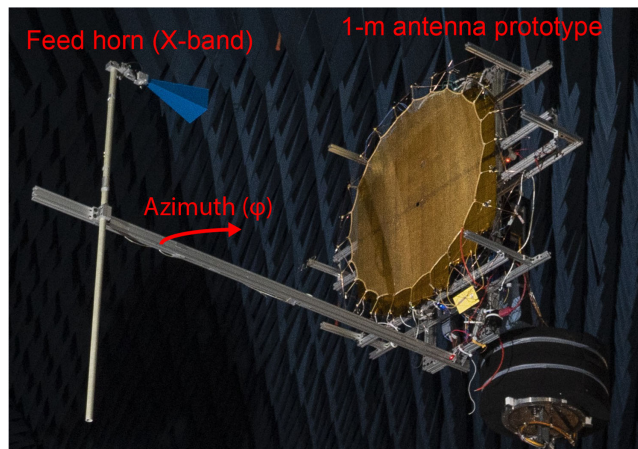


Fig. 8 Electrostatically actuated mesh reflector at the Compact Range Facility at MIT Lincoln Laboratory. Azimuth plane radiation patterns were measured at 10 GHz with a standard X-band feed horn.

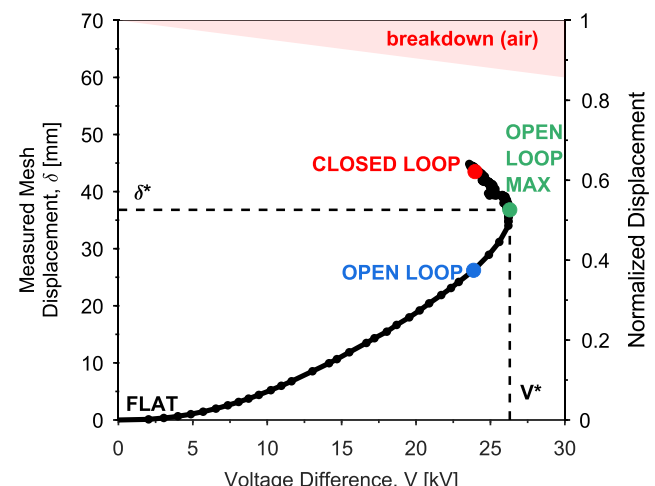


Fig. 9 Measured mesh displacement vs applied voltage difference between the mesh and command surfaces (V). The displacement increases rapidly with voltage near the pull-in instability ($V^* \approx 26.2$ kV, $\delta^* \approx 38$ mm), but is stabilized with closed-loop actuation. Arcing occurs at a mesh displacement of $\delta \approx 45$ mm.

closed-loop controller stabilized the system past pull-in. Comparing the pull-in curve of Fig. 9 with the membrane model of Sec. II.C, we see it follows a similar curve with distinct regions before and after the pull-in point. There is also reasonable agreement between the observed pull-in value and the predicted value of $\delta^* \approx 0.43d \approx 30$ mm.

We used stereo digital image correlation (DIC) to measure the mesh surface at the four points labeled in Fig. 9. Two 5-megapixel CMOS cameras (Imager M-lite) were used to capture images, which were filtered and processed with the LaVision StrainMaster software [36]. Using a zero-strain measurement, i.e., no imposed deformation, we found the worst-case displacement noise floor to be of order 1 mm. The results, summarized in Fig. 10 as contour plots and a profile cut through the nadir, show roughly parabolic surfaces and increasing mesh displacement with greater electrostatic actuation. The nadir of the mesh surface, which is not perfectly coincident with the laser measurement location, shifts slightly with increasing vertical displacement.

We measured radiation patterns under open- and closed-loop actuation in the azimuth range $\varphi \in [-30^\circ, 30^\circ]$. Given the mesh diameter of $D \approx 0.95$ m, the feed horn was placed at a focal distance of $f = 1.31$ m to achieve maximum gain when the center of the mesh was displaced to $\delta = 42.4$ mm, corresponding to a focal length-to-diameter ratio of $f/D = (D/16\delta) \approx 1.4$. The radiation patterns measured with this setup are plotted in Fig. 11. Table 2 summarizes the measured maximum gain and half-power beamwidth values. With no actuation, i.e., a flat mesh, we measured a low maximum gain and a defocused beam. However, as we increased the bias voltage and actuated the mesh into a curved surface, the gain increased and the beam came into focus. At the maximum mesh deflection of $\delta_{\max} = 42.35$ mm achieved with closed-loop actuation, we obtained the sharpest peak with a maximum gain of $G = 33.4$ dBi and a half-power beamwidth of $HPBW = 2.8^\circ$. For comparison, analytical estimates of gain and half-power beamwidth for a parabolic reflector at X-band, assuming an approximate efficiency of $\eta \approx 60\%$, are [37]

$$G^* = 10\log_{10}\left(\eta\left(\frac{\pi D}{\lambda}\right)^2\right) \approx 37.7 \text{ dBi} \quad (15)$$

$$HPBW^* = \frac{70\lambda}{D} \approx 2.2^\circ \quad (16)$$

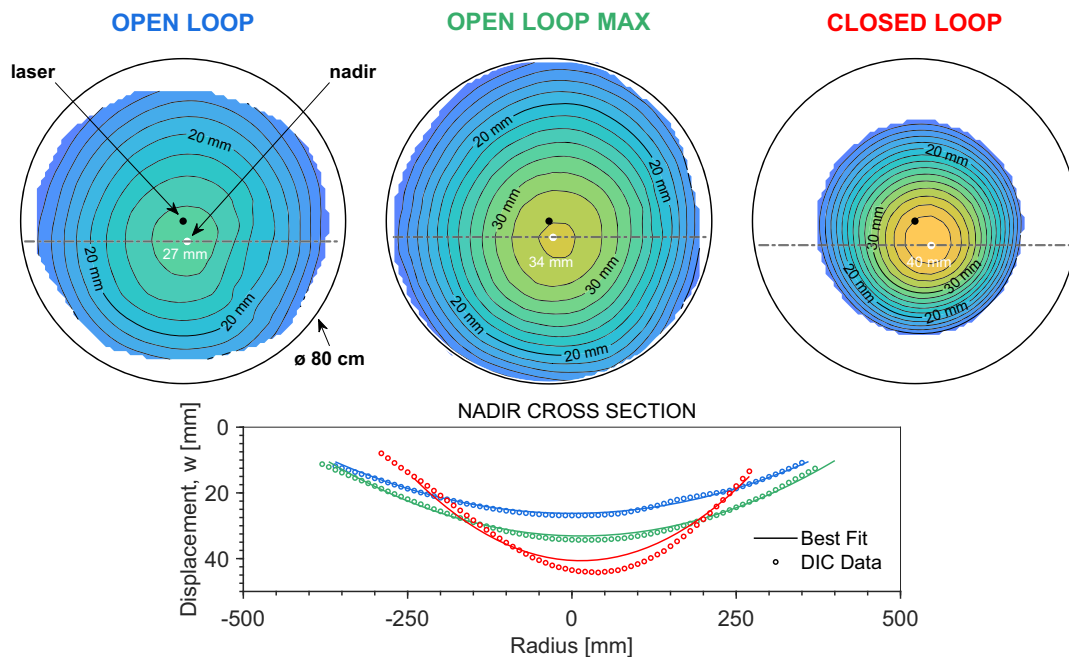


Fig. 10 Contour plots of the out-of-plane mesh deflection under open-loop and closed-loop electrostatic actuation, measured with stereo digital image correlation. The plot below compares the cross-sectional displacement through the nadir (indicated by the gray dashed line in the contour plots) with best-fit paraboloids.

The analytical estimates are reasonably close to the experimental results, given various potential sources for a reduced aperture efficiency, including surface error and excess spillover from the pyramidal horn, as indicated by the higher side lobes in the radiation patterns of Fig. 11.

We define two types of surface error that directly influence the RF pattern: i) random surface error, which enters Ruze's equation for RF loss [38], and ii) systematic error due to the nonlinear mechanics of electrostatic actuation as well as drift of the reflector surface toward the command surface. The high-sample-rate laser displacement sensors measured random surface error at a single point near the nadir. On short timescales, of order milliseconds to seconds, the temporal root mean square (RMS) surface error varied with test conditions (bias voltages, total deflection, humidity, among other variables), generally increasing with deflection. In favorable quiescent conditions, the temporal surface error was on the order of 100 μm . At the closed-loop set point, the worst-case temporal surface error was of order 2.2 mm. Using this value with Ruze's equation gives a loss of -3.7 dB, consistent with our experimental results.

The stereo DIC measurements were only able to assess systematic error, i.e., the deviation from a parabolic surface, because of the slow refresh rate and the poor spatial resolution of the windowing procedure used to image the porous mesh. The comparison of cross-sectional profiles of our reflector with best-fit paraboloids in Fig. 10 shows that the reflector is slightly conical, with a peak at the nadir. The deviation from an ideal paraboloid increases as the mesh is pulled deeper, due to the nonlinear electrostatic pressure term in Eq. (14). Additionally, on longer timescales, of order hours, the reflector often drifted toward the command surface. The main sources of this drift were viscoelastic creep of the catenary attachments, shifting of the support structure, and dielectric surface charging. The long timescale drift can be corrected with a closed-loop controller that adjusts the bias voltage.

The results of Fig. 11 demonstrate that the electrostatically actuated reflector prototype performs similarly to a parabolic reflector. Additionally, the decreasing beamwidth with increasing mesh displacement demonstrates that electrostatic actuation actively focuses the beam, which is pulled into focus as the mesh displaces toward the command surface. The obvious asymmetries in the RF pattern may have resulted from small variations in the initial gap distance as well as interference from the Bend-Formed support structure.

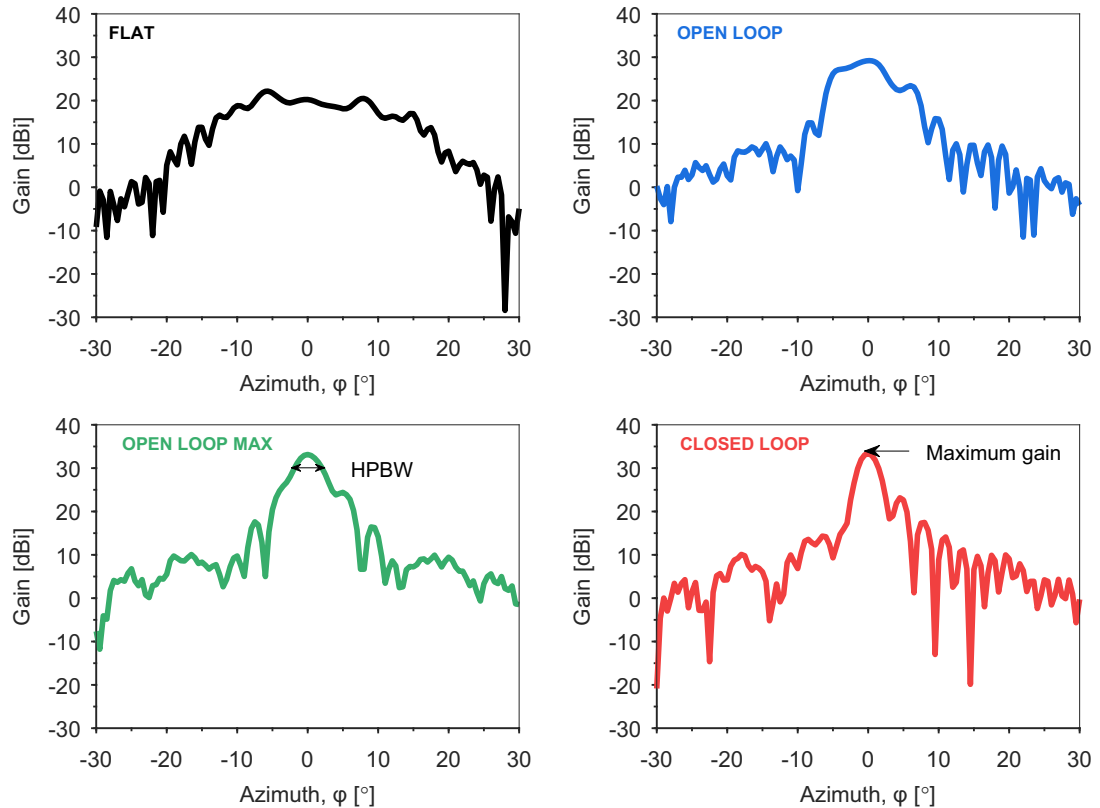


Fig. 11 Measured radiation patterns under open-loop and closed-loop electrostatic actuation, demonstrating focusing of the beam. A maximum gain of $G = 33.4$ dBi and half-power beamwidth of HPBW = 2.8° are measured with closed-loop actuation.

Table 2 Measured antenna performance for different mesh center displacements

Configuration	Mesh center displacement, mm	Maximum gain, dBi	HPBW, °
FLAT	0	22.1	—
OPEN LOOP	26	29.2	7.4
MAX OPEN LOOP	37	33.2	3.9
CLOSED LOOP	42	33.4	2.8

B. Beam Steering

The reflector prototype was also used to demonstrate beam steering via asymmetric electrostatic actuation. For large aperture reflectors, this capability eliminates the need to mechanically slew the entire reflector, which becomes difficult due to the large inertia, low damping, and low natural frequency of the support structure [39]. To demonstrate beam steering on our prototype, we connected the HV amplifier to one half of the command surface with the other side

grounded and varied the amplifier control voltage between $v_c \in [-5 \text{ kV}, 5 \text{ kV}]$, thereby adjusting the electrostatic force on half the mesh. In this configuration, the HV amplifier controls the voltage v_c on the command surface independent of the global bias voltage V_b .

Measurements of the reflector surface under asymmetric actuation, summarized in Fig. 12, show the nadir shifts by 5 cm as the amplifier voltage is increased from +1 to +5 kV. Implementing this asymmetric actuation in both directions at the maximum open-loop displacement of $\delta = 37 \text{ mm}$, we measured the radiation patterns shown in Fig. 13. These patterns clearly show the main lobe of the RF pattern shifting with the amplifier control voltage. The relationship between amplifier control voltage and beam shift, also plotted in Fig. 13, is linear with a slope of $0.42^\circ/\text{kV}$. The total angular range accessible through beam steering was $\Delta\phi = 4.2^\circ$. This range would enable an electrostatically actuated reflector antenna in geosynchronous orbit to scan across 2600 km, nearly the size of the contiguous United States. Further, by coupling this beam steering capability with active vibration suppression of the support structure, as described in [39], we can potentially scan the

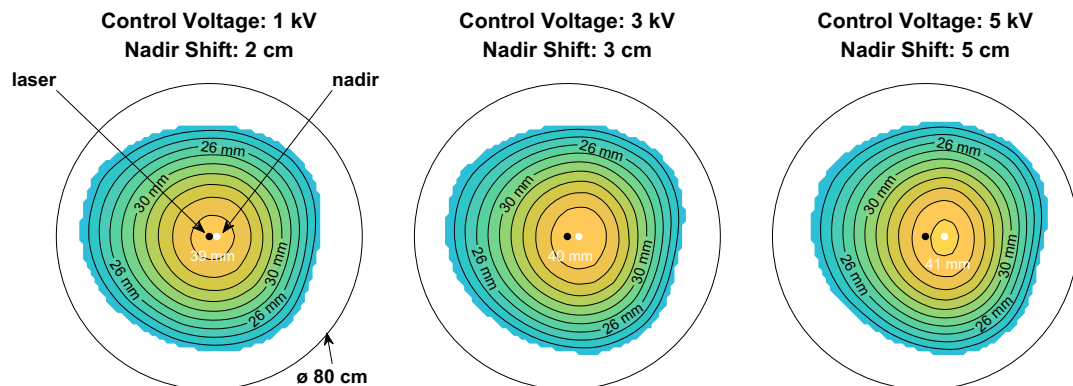


Fig. 12 Contour plots of the out-of-plane mesh deflection under beam steering, measured with stereo digital image correlation. The amplifier control voltages and resulting nadir shifts are labeled.

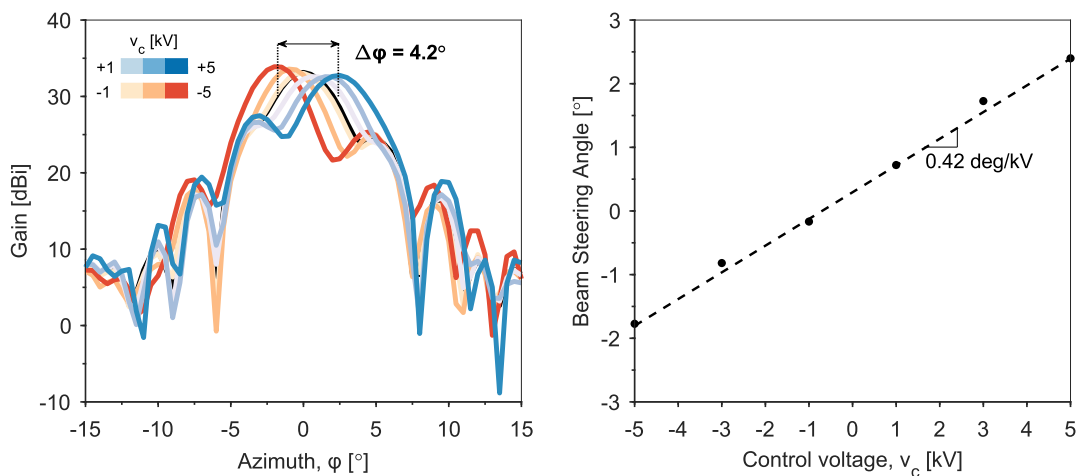


Fig. 13 Measured radiation patterns under beam steering and beam steering angle vs amplifier control voltage, demonstrating a maximum beam steering angle of $\Delta\varphi = 4.2^\circ$.

beam with rapid refresh rates for applications such as persistent real-time RF monitoring of storm systems.

IV. Conclusions

This paper presented a demonstration of an electrostatically actuated mesh reflector with a Bend-Formed support structure, potentially suitable for large aperture reflectors in space. This prototype was used to demonstrate open-loop, closed-loop, and asymmetric electrostatic actuation of the metallic mesh surface. The X-band radiation patterns showed similar performance to a parabolic reflector, with errors resulting from asymmetries in the deformation and interference from the support structures. The radiation patterns also demonstrated active focusing of the beam with open- and closed-loop actuation and beam steering of up to 4.2° with asymmetric actuation. These results establish the feasibility of using electrostatic actuation for forming a mesh reflector with advantages such as variable f/D and rapid beam steering—not easily achievable with previous technology. As metallic meshes are commonly used for deployable RF antennas in space, this prototype represents a novel architecture for achieving large reflectors by integrating a candidate ISM process with actively controlled mesh surfaces through electrostatic actuation.

Additional work is needed to de-risk certain aspects of the reflector concept presented here. For Bend-Forming, a major unresolved challenge is automating the attachment of joints, electrode booms, and mesh onto the support structure. Possible solutions include integrating the CFRP booms and metal struts into a single combined feedstock or using multiple formation-flying spacecraft for different aspects of the fabrication process, e.g., fabrication of the truss support structure, attachment of the joints, and final attachment of the mesh onto the ring truss. Another key challenge is attitude control during on-orbit fabrication due to large changes in inertial properties over long time scales of fabrication. We are currently investigating this topic to determine attitude control strategies for pointing important spacecraft subsystems like solar panels and communication antennas throughout the fabrication process.

For electrostatic actuation, future work should address the undesirable scaling of bias voltage with reflector size (cf. Sec. II.C) and space environment interactions. Using Eq. (9), the estimated voltage required to drive a 100-m-diam reflector with a flat command surface is of order 200 kV, which is excessively high. Candidate methods for reducing the voltage include preforming the mesh to lower the required electrostatic pressure or mechanically adjusting the gap distance between the command surface and the reflector. Another concern is space-environment interactions giving rise to leakage currents, which might saturate the power budget. These topics will be addressed in forthcoming papers.

Acknowledgements

This work was supported by the Under Secretary of Defense for Research and Engineering. The authors gratefully acknowledge funding from the MIT Lincoln Laboratory Advanced Concepts Committee and the Northrop Grumman Corporation. J.Z.Z. also acknowledges support from the National Science Foundation Graduate Research Fellowship Program (NSF GRFP) Grant No. 1745302. Special thanks to Christopher Churchill and Brian Tran, both of Northrop Grumman Corporation, for their assistance in designing and fabricating the mesh surface, and to Andy Kwas, whose vision and encouragement enabled this work.

Distribution Statement A

Approved for public release. Distribution is unlimited. This material is based upon work supported by the Department of the Air Force under Air Force Contract No. FA8702-15-D-0001. Any opinions, findings, conclusions, or recommendations expressed in this material are those of the author(s) and do not necessarily reflect the views of the Department of the Air Force. Delivered to the U.S. Government with Unlimited Rights, as defined in DFARS Part 252.227-7013 or 7014 (Feb 2014). Notwithstanding any copyright notice, U.S. Government rights in this work are defined by DFARS 252.227-7013 or DFARS 252.227-7014 as detailed above. Use of this work other than as specifically authorized by the U.S. Government may violate any copyrights that exist in this work. © 2023 Massachusetts Institute of Technology

References

- [1] Banik, J., "Realizing Large Structures in Space," *Frontiers of Engineering: Reports on Leading-Edge Engineering from the 2015 Symposium*, National Academies Press, Washington, D.C., 2016, pp. 55–62. <https://doi.org/10.17226/21825>
- [2] Thomson, M. W., "The AstroMesh Deployable Reflector," *IEEE Antennas and Propagation Society International Symposium*, Vol. 3, Inst. of Electrical and Electronics Engineers, New York, 1999, pp. 1516–1519. <https://doi.org/10.1109/APS.1999.838231>
- [3] Hedgepeth, J. M., "Influence of Fabrication Tolerances on the Surface Accuracy of Large Antenna Structures," *AIAA Journal*, Vol. 20, No. 5, 1982a, pp. 680–686. <https://doi.org/10.2514/3.7936>
- [4] Hedgepeth, J. M., "Accuracy Potentials for Large Space Antenna Reflectors with Passive Structure," *Journal of Spacecraft and Rockets*, Vol. 19, No. 3, 1982b, pp. 211–217. <https://doi.org/10.2514/3.62239>
- [5] "Northrup Grumman Astro Aerospace," AstroMesh, 2017, <https://www.northropgrumman.com/wp-content/uploads/AstroMesh-DataSheet.pdf>.
- [6] Rogers, C., Stutzman, W., Campbell, T., and Hedgepeth, J., "Technology Assessment and Development of Large Deployable Antennas,"

- Journal of Aerospace Engineering*, Vol. 6, No. 1, 1993, pp. 34–54.
[https://doi.org/10.1061/\(ASCE\)0893-1321\(1993\)6:1\(34\)](https://doi.org/10.1061/(ASCE)0893-1321(1993)6:1(34))
- [7] Thomson, M., “Astromesh Deployable Reflectors for Ku and Ka Band Commercial Satellites,” *20th AIAA International Communication Satellite Systems Conference and Exhibit*, AIAA Paper 2002-2032, 2002.
<https://doi.org/10.2514/6.2002-2032>
- [8] Taminger, K. M., and Hafley, R. A., “Electron Beam Freeform Fabrication (EBF3) for Cost Effective Near-Net Shape Manufacturing,” NASA TM-2006-214284, 2006, <https://ntrs.nasa.gov/citations/20080013538>
- [9] Kugler, J., Cherston, J., Joyce, E. R., Shestople, P., and Snyder, M. P., “Applications for the Archinaut In-Space Manufacturing and Assembly Capability,” *AIAA SPACE and Astronautics Forum and Exposition*, AIAA Paper 2017-5365, 2017.
<https://doi.org/10.2514/6.2017-5365>
- [10] Levedahl, B., Hoyt, R. P., Silagy, T., Gorges, J., Britton, N., and Slostad, J., “Trusselator™ Technology for In-Situ Fabrication of Solar Array Support Structures,” *2018 AIAA Spacecraft Structures Conference*, AIAA Paper 2018-2203, 2018.
<https://doi.org/10.2514/6.2018-2203>
- [11] Adams, E., and Irvine, C., “MSFC Evaluation of the Space Fabrication Demonstration System (Beam Builder),” NASA TM-82440, 1981, <https://ntrs.nasa.gov/citations/19820002206>.
- [12] Bhundiya, H. G., and Cordero, Z. C., “Bend-Forming: A CNC Deformation Process for Fabricating 3D Wireframe Structures,” *Additive Manufacturing Letters*, Vol. 6, July 2023, Paper 100146.
<https://doi.org/10.1016/j.addlet.2023.100146>
- [13] Bhundiya, H. G., Royer, F., and Cordero, Z., “Engineering Framework for Assessing Materials and Processes for In-Space Manufacturing,” *Journal of Materials Engineering and Performance*, Vol. 31, No. 8, 2022, pp. 6045–6059.
<https://doi.org/10.1007/s11665-022-06755-y>
- [14] Lang, J. H., and Staelin, D. H., “Electrostatically-Controlled Large-Aperture Reflecting Satellite Antennas,” *1980 19th IEEE Conference on Decision and Control Including the Symposium on Adaptive Processes*, Inst. of Electrical and Electronics Engineers, New York, 1980, pp. 991–993.
<https://doi.org/10.1109/CDC.1980.271950>
- [15] Lang, J., and Staelin, D., “The Computer-Controlled Stabilization of a Noisy Two-Dimensional Hyperbolic System,” *IEEE Transactions on Automatic Control*, Vol. 27, No. 5, 1982, pp. 1033–1043.
<https://doi.org/10.1109/TAC.1982.1103073>
- [16] Yam, Y., Lang, J., Staelin, D., and Johnson, T., “The Experimental Computer Control of a Two-Dimensional Hyperbolic System,” *IEEE Transactions on Automatic Control*, Vol. 33, No. 1, 1988, pp. 79–87.
<https://doi.org/10.1109/9.363>
- [17] Mihora, D. J., and Redmond, P. J., “Electrostatically Formed Antennas,” *Journal of Spacecraft and Rockets*, Vol. 17, No. 5, 1980, pp. 465–473.
<https://doi.org/10.2514/3.57766>
- [18] Chodimella, S., Moore, J., Otto, J., and Fang, H., “Design Evaluation of a Large Aperture Deployable Antenna,” *47th AIAA/ASME/ASCE/AHS/ASC Structures, Structural Dynamics, and Materials Conference*, AIAA Paper 2006-1603, 2006.
<https://doi.org/10.2514/6.2006-1603>
- [19] Clarricoats, P., and Zhou, H., “Design and Performance of a Reconfigurable Mesh Reflector Antenna. Part 1: Antenna Design,” *IEE Proceedings H (Microwaves, Antennas and Propagation)*, Vol. 138, Inst. of Electrical Engineers, London, U.K., 1991, pp. 485–492.
<https://doi.org/10.1049/ip-h-2.1991.0082>
- [20] Washington, G., “Active Aperture Antennas,” *ASME International Mechanical Engineering Congress and Exposition*, Vol. 15373, American Soc. of Mechanical Engineers, Fairfield, NJ, 1996, pp. 505–509.
- [21] Fernández, E. J., and Artal, P., “Membrane Deformable Mirror for Adaptive Optics: Performance Limits in Visual Optics,” *Optics Express*, Vol. 11, No. 9, 2003, pp. 1056–1069.
<https://doi.org/10.1364/OE.11.001056>
- [22] Gorinevsky, D., and Hyde, T. T., “Adaptive Membrane for Large Lightweight Space Telescopes,” *Highly Innovative Space Telescope Concepts*, Vol. 4849, Soc. of Photo-Optical Instrumentation Engineers, Bellingham, WA, 2002, pp. 330–338.
<https://doi.org/10.1117/12.460076>
- [23] Wang, X., Knapp, P., Vaynman, S., Graham, M., Cao, J., and Ulmer, M., “Experimental Study and Analytical Model of Deformation of Magnetostrictive Films as Applied to Mirrors for X-Ray Space Telescopes,” *Applied Optics*, Vol. 53, No. 27, 2014, pp. 6256–6267.
<https://doi.org/10.1364/AO.53.006256>
- [24] Peng, F., Jiang, X.-X., Hu, Y.-R., and Ng, A., “Application of Shape Memory Alloy Actuators in Active Shape Control of Inflatable Space Structures,” *2005 IEEE Aerospace Conference*, Inst. of Electrical and Electronics Engineers, New York, 2005, pp. 1–10.
- [25] Niewiarowski, A., Adriaenssens, S., and Pauletti, R. M., “Adjoint Optimization of Pressurized Membrane Structures Using Automatic Differentiation Tools,” *Computer Methods in Applied Mechanics and Engineering*, Vol. 372, Dec. 2020, Paper 113393.
<https://doi.org/10.1016/j.cma.2020.113393>
- [26] DeTienne, M. D., Brucolieri, A. R., Molnar-Fenton, A., Chalifoux, B., Heilmann, R. K., Yao, Y., and Schattenburg, M. L., “X-Ray Telescope Mirror Mounting and Deformation Reduction Using ThermoYield Actuators and Mirror Geometry Changes,” *Space Telescopes and Instrumentation 2018: Ultraviolet to Gamma Ray*, Vol. 10699, Soc. of Photo-Optical Instrumentation Engineers, Bellingham, WA, 2018, pp. 1029–1043.
<https://doi.org/10.1117/12.2314896>
- [27] Labs, P., “D.I. Wire Pro Info,” 2022, <https://aetlabs.com/wp-content/uploads/D.I.WireProInfo.pdf> [retrieved 8 Sept. 2023].
- [28] Haus, H. A., and Melcher, J. R., *Electromagnetic Fields and Energy*, Vol. 107, Prentice-Hall, Upper Saddle River, NJ, 1989, pp. 37–38.
- [29] Royer, F., and Pellegrino, S., “Ultralight Ladder-Type Coilable Space Structures,” *2018 AIAA Spacecraft Structures Conference*, AIAA Paper 2018-1200, 2018.
<https://doi.org/10.2514/6.2018-1200>
- [30] Schlothauer, A., Royer, F., Pellegrino, S., and Ermanni, P., “Flexible Silicone Molds for the Rapid Manufacturing of Ultra-Thin Fiber Reinforced Structures,” *SAMPE Conference Proceedings*, Soc. for the Advancement of Material and Process Engineering, North America, May 2018, [https://www.researchgate.net/profile/Arthur-Schlothauer/publication/325781102_Flexible_Silicone_Molds_For_the_Rapid_Manufacturing_of_Utra-Thin_Fiber_Reinforced_Structures/links/617a69493c987366c3f4dcf9/Flexible-Silicone-Molds-For-the-Rapid-Manufacturing-of-Utra-Thin_Fiber_Reinforced-Structures.pdf](https://www.researchgate.net/profile/Arthur-Schlothauer/publication/325781102_Flexible_Silicone_Molds_For_the_Rapid_Manufacturing_of_Ultra-Thin_Fiber_Reinforced_Structures/links/617a69493c987366c3f4dcf9/Flexible-Silicone-Molds-For-the-Rapid-Manufacturing-of-Ultra-Thin-Fiber-Reinforced-Structures.pdf).
- [31] Hayden, J., “The Dielectric Strength of the Vacuum: Electrostatic Ionization Gradient of Metal Electrodes,” *Journal of the American Institute of Electrical Engineers*, Vol. 41, No. 11, 1922, pp. 852–853.
<https://doi.org/10.1109/JoAIEE.1922.6591649>
- [32] Zhang, W.-M., Yan, H., Peng, Z.-K., and Meng, G., “Electrostatic Pull-In Instability in MEMS/NEMS: A Review,” *Sensors and Actuators A-Physical*, Vol. 214, Aug. 2014, pp. 187–218.
<https://doi.org/10.1016/j.sna.2014.04.025>
- [33] Joseph, D. D., and Lundgren, T. S., “Quasilinear Dirichlet Problems Driven by Positive Sources,” *Archive for Rational Mechanics and Analysis*, Vol. 49, Jan. 1973, pp. 241–269.
<https://doi.org/10.1007/BF00250508>
- [34] Pelesko, J., and Chen, X., “Electrostatic Deflections of Circular Elastic Membranes,” *Journal of Electrostatics*, Vol. 57, No. 1, 2003, pp. 1–12.
[https://doi.org/10.1016/S0304-3886\(02\)00073-6](https://doi.org/10.1016/S0304-3886(02)00073-6)
- [35] Pelesko, J. A., and Driscoll, T. A., “The Effect of the Small-Aspect-Ratio Approximation on Canonical Electrostatic MEMS Models,” *Journal of Engineering Mathematics*, Vol. 53, Dec. 2005, pp. 239–252.
<https://doi.org/10.1007/s10665-005-9013-2>
- [36] “2D/3D Stereo DIC–StrainMaster,” LaVision, 2022, <https://www.lavision.de/en/products/strainmaster/index.php> [retrieved 8 Sept. 2023].
- [37] Minoli, D., *Satellite Systems Engineering in An IPv6 Environment*, Auerbach Publ., 2009.
- [38] Welch, B. W., “Application of Ruze Equation for Inflatable Aperture Antennas,” NASA TP-2008-214953, 2008.
- [39] Angeletti, F., Iannelli, P., Gasbarri, P., and Sabatini, M., “End-to-End Design of a Robust Attitude Control and Vibration Suppression System for Large Space Smart Structures,” *Acta Astronautica*, Vol. 187, Oct. 2021, pp. 416–428.
<https://doi.org/10.1016/j.actaastro.2021.04.007>

M. A. Ayoubi
Associate Editor